NANO LETTERS

pubs.acs.org/NanoLett Letter

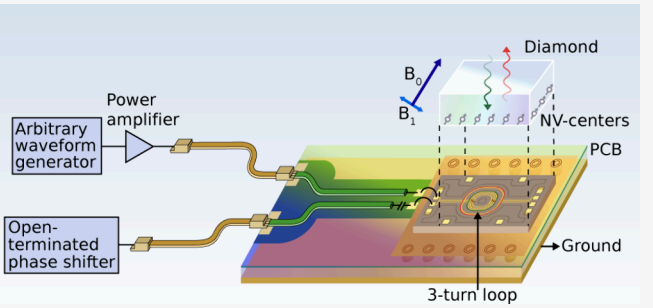
# Impedance-Tuned Microwave Loop for Fast, Homogeneous Rabi Oscillations of a Dense Ensemble of NV-Diamond Electronic Spins

Han Sae Jung, Johannes Cremer, Aoyang Zhang, Shuhao Fan, Sangha Kim, Guang Yang, Ronald L. Walsworth,* and Donhee Ham*

Cite This: *Nano Lett.* 2025, 25, 15566−15571 Read Online

ACCESS | Metrics & More | Article Recommendations | Supporting Information

**ABSTRACT:** Obtaining a high Rabi oscillation frequency homogeneously across a spatially extended population of nitrogen-vacancy (NV) center electronic spins in diamond is useful for efficient spin-state manipulation of the NV ensemble and in using NVs to detect ensembles of other spin species. Here, we achieve a high, homogeneous Rabi frequency for a dense NV ensemble by enhancing the microwave magnetic fields in the center region of a diamond-coupled planar metallic loop via systematic engineering that increases the microwave current driving of the loop, while avoiding off-center proximity to the loop that gives strong but inhomogeneous microwave fields. With such enhanced microwave fields at 2.55 GHz, we achieve a 136.3 MHz NV Rabi frequency with 1.5% inhomogeneity over a 40 $\mu$m × 40 $\mu$m diamond area, and we use the NV ensemble to detect a ∼30-MHz magnetic signal, similar to a nuclear magnetic resonance (NMR) signal at a tesla-scale bias magnetic field, with Hz-scale spectral resolution.




**KEYWORDS:** *Nitrogen-vacancy center, diamond, electron spins, Rabi oscillation, quantum coherence, microwave engineering, nuclear magnetic resonance*

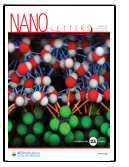
Downloaded via UNIV OF MARYLAND COLG PARK on November 17, 2025 at 23:34:40 (UTC).
See https://pubs.acs.org/sharingguidelines for options on how to legitimately share published articles.

Electronic spin dynamics in diamond nitrogen-vacancy (NV) centers can have sufficient quantum coherence[1,2] to exhibit Rabi oscillations when driven by a GHz microwave magnetic field tuned to the NV electron spin resonance (ESR) frequency $f_0$.[2,3] Increasing the NV Rabi oscillation frequency $f_1$ is often desired, because a larger $f_1$ for a given spin dephasing time allows a greater number of quantum-coherent manipulations.[3] Since $f_1 = \gamma B_1/2^{1/2}$ where $B_1$ is the amplitude of the linearly driving microwave magnetic field and $\gamma$ is the electron gyromagnetic ratio,[3] obtaining a larger $f_1$ amounts to driving a conducting wire or antenna with a larger-amplitude GHz current to produce a stronger $B_1$. However, increasing the driving current at GHz frequencies is generally a nontrivial task in microwave engineering.[3−7]

Certain applications with NV electronic spins not only benefit from a high $f_1$ but actually require a minimum $f_1$. A case in point is the measurement of nuclear magnetic resonance (NMR) signals—nuclear spin precession—using NV electronic spin dynamics as the detector.[8−12] In this "NV-NMR" scheme, particularly in protocols based on pulsed dynamical decoupling, NV electronic spins can sense the frequency and phase of nuclear spin precession via dipole−dipole coupling, with the NV dynamics read out optically. A key requirement for such NV-NMR measurements is that $f_1$ must be significantly larger than the NMR frequency, $f_{NMR}$, i.e., the nuclear spin precession frequency. NV-NMR can offer higher sensitivity for small samples than traditional inductive NMR, enabling spectroscopy at the nano and microscale.[8−12] However, this advantage comes with the challenge that the requirement $f_1 > f_{NMR}$ becomes increasingly stringent as the static magnetic field $B_0$ is raised to achieve higher NMR spectral resolution. Since increasing $B_0$ raises both $f_0$ and $f_{NMR}$, the minimum $f_1$ required also increases. Meeting this requirement demands driving a conducting wire with a larger current amplitude at a higher GHz frequency ($f_0$), working against the general trend that microwave driving becomes more difficult at higher frequency. For this reason, the high-resolution NMR readily achieved with inductive readout, e.g., commercial 300−600 MHz $^1$H NMR at $B_0 \approx 7.1$−14.1 T, remains well beyond the current reach of NV-NMR.

Thus, whether for NV-NMR or for other applications, substantial research has been devoted to increasing $f_1$ for NV electronic spins.[3−7] In particular, large $B_1$ can be readily attained at GHz ESR frequencies using a wire loop, even without excessive current, at positions proximate to the wire

**Received:** July 23, 2025
**Revised:** September 26, 2025
**Accepted:** October 13, 2025
**Published:** October 16, 2025



ACS Publications © 2025 American Chemical Society

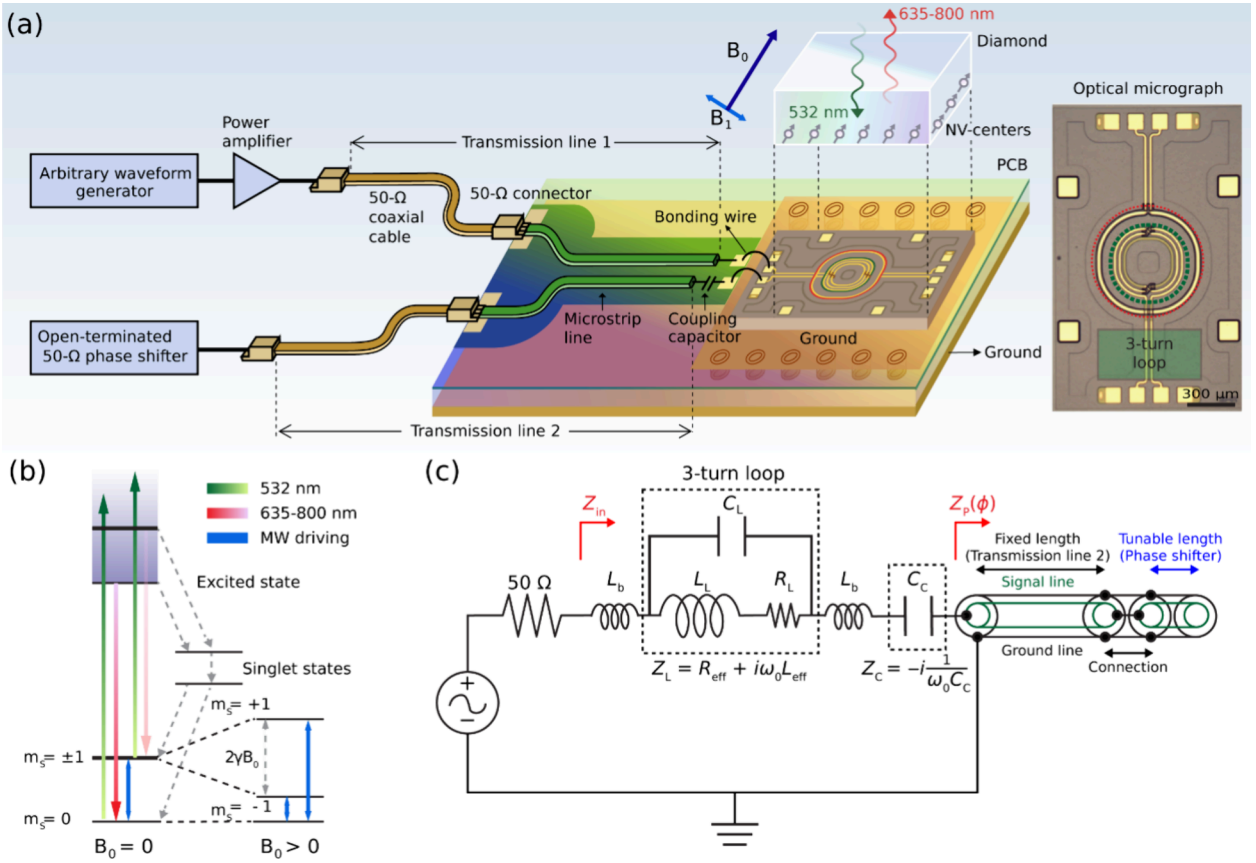



**Figure 1.** (a) Schematic of the device and measurement setup showing the full microwave path (left); optical image of the chip featuring the 3-turn planar Cu loop (right). The diamond is mounted on the chip so that its NV-rich ∼10 $\mu$m layer faces the loop. The 3-turn loop (dashed green circle, right) serves as the microwave antenna; the additional single loop (dashed red circle, right) is left open-circuited and unused. (b) NV electronic spin states, optical and microwave transitions, and dependence on $B_0$. (c) Circuit model of the microwave path (Transmission line 1 is omitted, since the 50-Ω microwave source is matched to 50-Ω Transmission line 1). For maximal current delivery into the loop, $|Z_{in}|$ should be minimized (ideally to zero) by properly choosing $C_C$ and $\phi$.

rather than at the loop center. As an extreme example, exploiting such edge fields yielded $f_1$ = 0.44 GHz at $f_0$ = 0.49 GHz ($f_1/f_0 \approx 0.90$), albeit with significant $B_1$ inhomogeneity.[3] These edge regions remain useful for applications involving a small number of NVs localized within <1 $\mu$m, but they are unsuitable for applications that require a spatially extended NV ensemble (>1 $\mu$m), such as micrometer-scale NV-NMR.[8−12] For such applications, which demand greater $B_1$ and $f_1$ homogeneity, the loop center region is preferable; because $B_1$ is minimum at the center and increases radially outward, it is maximally homogeneous around the center. At the same time, because $B_1$ is lowest at the center, achieving a high target $B_1$ or $f_1$ is more difficult, requiring delivery of a larger-amplitude microwave current into the loop. For example, the work reported in ref 4 achieved millimeter-scale $B_1$ inhomogeneity of less than 5% (normalized standard deviation) at $f_0$ = 2.87 GHz in the loop center region, but the resulting $f_1$ value was only 14.3 MHz ($f_1/f_0 \approx 5.0 \times 10^{-3}$).

Here, we report strong yet homogeneous quantum-coherent manipulation of a large ensemble of NV electronic spins at GHz ESR frequencies, achieved through systematic microwave engineering that enhances the microwave current driving of a 3-turn planar loop coupled to a diamond (the "device"). Within a 40 $\mu$m × 40 $\mu$m diamond area in the loop center region, we achieve $f_1$ = 136.3 MHz at $f_0$ = 2.55 GHz ($f_1/f_0 \approx 5.3 \times 10^{-2}$) with $B_1$ inhomogeneity of ∼1.5% (normalized standard deviation). This result supports our long-term aim of high-resolution NV-NMR spectroscopy at tesla-scale bias magnetic fields, since the demonstrated 40 $\mu$m × 40 $\mu$m homogeneous region is on par with the analyte size of NV-NMR targets.[10−12] Moreover, we demonstrate NV-ensemble-based detection of a ∼30 MHz magnetic signal (similar to an NMR signal at ∼0.7 T bias field) using the device.

Our device consists of a thin slab of diamond (2.0 mm × 2.0 mm × 0.5 mm) mounted on four Cu support pads of a chip that features the 3-turn Cu microwave loop (Figure 1a, right). The support pads protrude slightly, leaving a micrometer-scale gap above the loop—unused in this work but available for future sample integration. The diamond slab fully covers the loop. We first describe the diamond sample and then the microwave loop. The surface of the diamond facing the loop embeds an ensemble of NV centers within a ∼10-$\mu$m depth. The NV-enriched layer is grown using chemical vapor deposition with isotopically purified $^{15}$N and contains 99.99% $^{12}$C (∼0.01% $^{13}$C) and 17 ppm $^{15}$N, yielding ∼2.7 ppm of NV$^-$ concentration. The measured NV electron spin dephasing times are ∼7.1 $\mu$s for a Hahn-Echo sequence and ∼33.0 $\mu$s for an XY8-6 sequence. In a static (bias) magnetic field, $B_0$, two ESR frequencies arise: $f_0 = \Delta + \gamma B_0$ for the $m_s = 0 \leftrightarrow +1$ transition, and $f_0 = |\Delta - \gamma B_0|$ for the $m_s = 0 \leftrightarrow -1$ transition, with $\Delta \approx 2.87$ GHz due to the zero-field splitting (Figure 1b). The microwave drive can be tuned to either ESR transition to


https://doi.org/10.1021/acs.nanolett.5c03811
Nano Lett. 2025, 25, 15566−15571

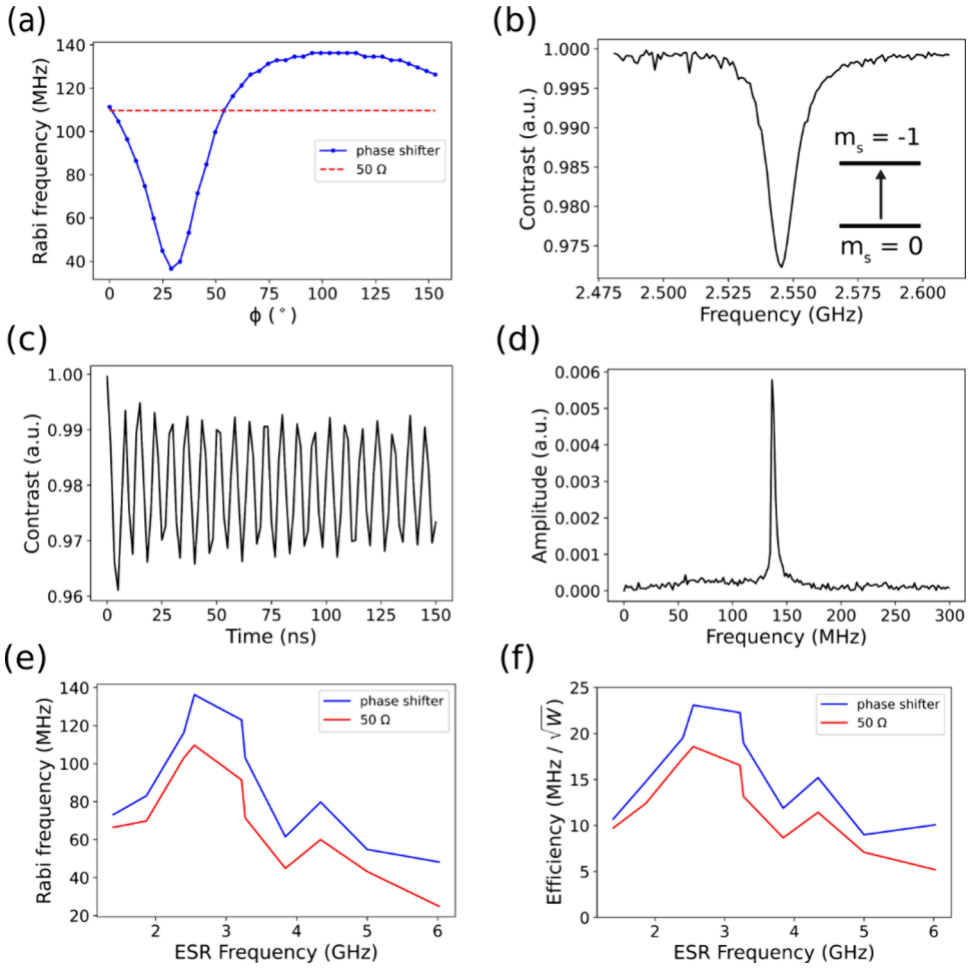



**Figure 2.** (a) NV-measured $f_1$ at the loop center vs $\phi$ (blue) and with fixed 50-Ω termination (red), at $f_0$ = 2.55 GHz for the splitting between $m_s$ = 0 and $m_s$ = −1 ($B_0$ = 116 G). At $\phi \approx 100°$, $f_1$ is maximized at 136.3 MHz. (b−d) Example ODMR spectrum, Rabi oscillation, and Fourier transform of the Rabi oscillation with a single peak at $f_1$ = 136.3 MHz, all for $\phi \approx 100°$ and $f_0$ = 2.55 GHz. (e) Maximum $f_1$ at the loop center obtained by $\phi$ tuning (blue) in comparison to $f_1$ at fixed 50-Ω termination (red) for a number of different $f_0$ values between 1.40 GHz and 6.02 GHz. (f) Repetition of (e) for driving efficiency, defined as the ratio of $f_1$ to the square root of the output power from the power amplifier.

induce Rabi oscillations between the corresponding NV spin states. In our setup, the NV centers have their quantization axis tilted 54.7° relative to the chip normal, and all values of $B_0$ and $B_1$ given throughout this paper are referenced to this NV axis: $B_0$ is the projection of the permanent-magnet field onto the NV axis (hence, tunable by adjusting the magnet's position and orientation); $B_1$ is the projection of the loop-produced microwave field onto the plane perpendicular to the NV axis. Optical initialization of NV spins into the $m_s$ = 0 state, and subsequent optical readout of Rabi oscillations during microwave driving, follow standard protocol (Figure 1b; see the Methods section in the Supporting Information; also see Figure S1 for the optics setup).[10−12]

We now describe the 3-turn loop. The 3 Cu turns (diameters 300 μm, 360 μm, and 420 μm; width 17 μm; effective thicknesses of 3 μm, ∼9 μm, and ∼9 μm; turn-to-turn gap = 13 μm; see Figure S2) are realized within a metallization stack framework, largely embedded in dielectric atop a 75-μm-thick semi-insulating SiC substrate, with partial exposure to air. The bottom of the chip is finished with a 10-μm-thick Au layer. The loop chip is designed by us, fabricated at a foundry, and packaged by us (see the Methods section).

The equivalent circuit of the loop (Figure 1c, dashed box) consists of an inductance $L_L$ in series with a parasitic resistance $R_L$, with this series branch in parallel with a parasitic capacitance $C_L$. The dominant contribution to $C_L$ is expected to come from interturn coupling, although smaller parasitic capacitances (e.g., to ground) are effectively absorbed into $C_L$. This simplified model largely reproduces the loop behavior observed in simulations (Figure S3). The self-resonance frequency of the loop is $f_{SRF} = (2\pi)^{-1}(L_L C_L)^{-1/2}$ and the loop impedance at the excitation frequency is $Z_L = (R_L + i\omega_0 L_L)||(i\omega_0 C_L)^{-1} \equiv R_{eff} + i\omega_0 L_{eff}$, where $L_{eff} \approx L_L[1 - (\omega_0/\omega_{SRF})^2]^{-1}$ and $R_{eff} \approx R_L[1 - (\omega_0/\omega_{SRF})^2]^{-2}$ are the frequency-dependent effective loop inductance and resistance ($\omega_0 = 2\pi f_0$; $\omega_{SRF} = 2\pi f_{SRF}$). For efficient operation, $f_0 < f_{SRF}$ should hold, under which the inductive ($L_L$) branch dominates and the loop behaves inductively ($L_{eff} > 0$), efficiently generating the microwave magnetic field. In contrast, for $f_0 > f_{SRF}$, the capacitive ($C_L$) branch dominates, the loop becomes capacitive ($L_{eff} < 0$), and magnetic field generation becomes inefficient. Fewer turns increase $f_{SRF}$ by reducing $C_L$ but weakens $B_1$ for a given current. The chosen 3-turn loop geometry balances this tradeoff, with the loop diameter further chosen to balance field strength against homogeneity.

Simulations (Figure S3) yield $L_L \approx 4.25$ nH, $R_L \approx 3.0$ Ω, and $C_L \approx 0.23$ pF, together with $f_{SRF} \approx 5.1$ GHz. Thus, the main excitation frequency in this work, $f_0$ = 2.55 GHz, lies


https://doi.org/10.1021/acs.nanolett.5c03811
Nano Lett. 2025, 25, 15566−15571

below $f_{SRF} \approx 5.1$ GHz. At $f_0 = 2.55$ GHz, $Z_L \approx 5.4 + 90.7i\ \Omega$ with $R_{eff} \approx 5.4\ \Omega$ and $L_{eff} \approx 5.7$ nH, which is inductive as expected, with a quality factor $Q = \omega_0 L_{eff}/R_{eff} \approx 17$. Of note, the chip also includes an additional single loop surrounding the 3-turn loop (Figure 1a, right), designed as a secondary shim. However, when driven, it coupled strongly to the primary loop, so it is left open-circuited and unused. Simulations confirm that in this open state, it has negligible effect on the primary loop (Figure S3).

The full microwave signal path is shown in Figure 1a, with its circuit model in Figure 1c. The chip with the diamond on top is mounted on a printed circuit board (PCB). One end of the loop is wire-bonded to "Transmission line 1" (a 50-Ω PCB microstrip plus a 50-Ω coaxial cable) connected to a microwave source (an arbitrary waveform generator followed by a 50-Ω power amplifier, ZHL-25W-63+). The other loop end is wire-bonded to a coupling capacitor $C_C$ in series with "Transmission line 2" (another 50-Ω PCB microstrip plus another 50-Ω coax) connected to an open-terminated 50-Ω phase shifter. The chip's gold backside is glued to the PCB ground plane.

In the circuit model (Figure 1c), the input impedance seen by the source is $Z_{in} = R_{eff} + i\omega_0(2L_b + L_{eff}) - i(\omega_0 C_C)^{-1} + Z_P(\phi)$, where $L_b$ is the inductance of each bond wire, estimated as $L_b \approx 1$ nH, and $Z_P(\phi)$ is the impedance presented by Transmission line 2 (with fixed phase delay $\phi_0$) plus the open-terminated phase shifter with a tunable phase delay $\phi$. If Transmission line 2 and the phase shifter are lossless, $Z_P(\phi) = -iZ_0 \times \cot(\phi + \phi_0)$ ($Z_0 = 50\ \Omega$), which spans $-\infty$ to $+\infty$ as $\phi$ varies, although, in practice, losses limit the span. The goal is then to choose $C_C$ and $\phi$ to minimize $|Z_{in}|$ (ideally to zero; intentionally mismatched from the source 50-Ω impedance) to maximize microwave current into the loop and, hence, $f_1$. At $f_0 = 2.55$ GHz, simulations estimate $R_{eff} + i\omega_0(2L_b + L_{eff}) \approx 5.4 + 123i\ \Omega$, so choosing $C_C = 0.5$ pF makes its capacitance impedance $-i(\omega_0 C_C)^{-1}$ nearly cancel the simulated $123i\ \Omega$ inductive term, yielding $Z_{in} \approx 5.4 - 2.1i + Z_P(\phi)$. If $\phi$ is then tuned so that $Z_P(\phi) \approx 2.1i$, $Z_{in}$ becomes purely real, minimizing $|Z_{in}|$ to 5.4 Ω.

In this ideal consideration, where $L_b$ and $L_{eff}$ are assumed known a priori so that $C_C$ cancels the inductive impedance almost exactly (from $123i\ \Omega$ to $-2.1i\ \Omega$), $Z_P(\phi)$ tuning would not be essential. One could simply ground the far side of the coupling capacitor and accept $Z_{in} \approx 5.4 - 2.1i$, giving $|Z_{in}| = 5.8\ \Omega$, which is already close to the theoretical minimum of 5.4 Ω. In practice (including our present case), however, $L_b$ and $L_{eff}$ cannot be predicted with perfect accuracy. Achieving near-zero cancellation of the inductive impedance with $C_C$ alone is therefore challenging, and the residual reactance may be substantially greater than $-2.1i$ and not negligible. In this situation, $Z_P(\phi)$ tuning provides a valuable adjustment, allowing residual reactance to be nulled and $|Z_{in}|$ minimized.

Moreover, $Z_P(\phi)$ tuning extends the operational range of $f_0$ around 2.55 GHz. Because $C_C$ is fixed at 0.5 pF (optimized for $f_0 = 2.55$ GHz), the imbalance between inductive and capacitive impedances grows as $f_0$ deviates from 2.55 GHz. In such case, $Z_P(\phi)$ supplies the additional reactive impedance needed to cancel the mismatch and minimize $|Z_{in}|$, provided the mismatch lies within the finite span of $Z_P(\phi)$ set by losses in Transmission line 2 and the phase shifter.

Figure 2a shows NV measurements of $f_1$ at the loop center vs $\phi$ (blue), juxtaposed with $f_1$ measured at the loop center with a fixed 50-Ω load replacing the phase shifter (red; see Figure S4 for its circuit diagram), where $f_0 = 2.55$ GHz for the $m_s = 0 \leftrightarrow -1$ transition ($B_0 = 116$ G in the present experiment). The $\phi$ scan yields $f_1$ values both above and below the fixed-load $f_1$ value, demonstrating that $|Z_{in}|$—and, thus, delivered current—varies widely with $\phi$ (see Figure S5 for impedance measurements). At $\phi \approx 100°$, $f_1$ reaches the maximum of 136.3 MHz, a notably high NV Rabi frequency measured at the loop center (Table S1). At this $\phi$ value, which minimizes $|Z_{in}|$, $Z_P(\phi)$ removes the residual reactance that $C_C = 0.5$ pF could not fully cancel.

Under the optimal $\phi \approx 100°$ at $f_0 = 2.55$ GHz, Figure 2b shows the NV optically detected magnetic resonance (ODMR) spectrum (i.e., optically detected ESR spectrum) while Figure 2c shows a representative Rabi oscillation; Figure 2d displays the Fourier transform of the Rabi oscillation with a single peak at $f_1 = 136.3$ MHz (see Figure S6 for different $f_0$ values). The ~3 MHz $^{15}$N hyperfine splitting (Figure S7) is power-broadened and unobserved in Figure 2b; and neither of the two associated detuned Rabi frequencies differ from $f_1 = \gamma B_1/2^{1/2} = 136.3$ MHz by less than 0.05%, because $f_1 \gg 3$ MHz, so they merge into a single $f_1$ peak in Figure 2d.

Figure 2e plots the maximum $f_1$ (Rabi frequency) at the center of the loop obtained by $\phi$ tuning alongside $f_1$ with a fixed 50-Ω load for a number of $f_0$ values between 1.40 and 6.02 GHz. As at $f_0 = 2.55$ GHz, optimal tuning drives a faster Rabi oscillation than the fixed-load case. The corresponding driving efficiency, defined as the ratio of $f_1$ to the square root of the output power from the power amplifier, is likewise higher for the optimally tuned configuration for all tested $f_0$ (Figure 2f; see also Figure S8). Figure 2e shows that, as $f_0$ moves away from 2.55 GHz, $f_1$ tends to decrease because $C_C = 0.5$ pF is optimized for $f_0 = 2.55$ GHz and residual mismatch between inductive and capacitive impedances at $f_0$ other than 2.55 GHz may exceed the finite span of $Z_P(\phi)$. Also, note that $f_1$ is substantially smaller for $f_0$ beyond $f_{SRF} \approx 5.1$ GHz, as expected.

At $f_0 = 2.55$ GHz, with the $\phi$ tuned for the maximal $f_1$ of 136.3 MHz at the loop center, the 3-turn loop delivers not only strong but also homogeneous microwave $B_1$ around the loop center. Figure 3a shows the $f_1$ map (equivalently a $B_1$ map, since $f_1 \propto B_1$) measured with the NV ensemble across a 280 $\mu$m × 280 $\mu$m area surrounding the innermost turn, using a scanned 5-$\mu$m diameter laser spot and a 10-$\mu$m pixel pitch. Within a 40 $\mu$m × 40 $\mu$m central region, $B_1$ shows little inhomogeneity, and measured NV Rabi oscillations at each point within this area are slowly damped, with Fourier spectra displaying a single, sharp peak (Figure S9). Across a larger 100 $\mu$m × 100 $\mu$m region (Figure 3b), $B_1$ variations increase, with Rabi oscillations more rapidly damped and Fourier spectra correspondingly broadened, at each measurement point outside the 100 $\mu$m × 100 $\mu$m area (Figure S9). Quantitatively, the mean $f_1$ is 139.3 and 150.3 MHz, with normalized standard deviations of about 1.5% and 6.3% within the 40 $\mu$m × 40 $\mu$m and 100 $\mu$m × 100 $\mu$m areas, respectively (Figure 3c). This $B_1$ homogeneity within the 40 $\mu$m × 40 $\mu$m NV-diamond area is expected to be sufficient for high-resolution, tesla-scale NV-NMR spectroscopy of a picoliter-scale analyte.[10−15] Equivalent measurements at $f_0 = 6.02$ GHz, above the loop's self-resonance frequency $f_{SRF}$, are shown in Figure S10.

Finally, we use our device to detect a 29.992 MHz radio frequency (RF) magnetic field signal generated by a test coil to emulate a tesla-scale NMR signal. The RF test signal is measured by the NV ensemble using coherently averaged


https://doi.org/10.1021/acs.nanolett.5c03811
Nano Lett. 2025, 25, 15566−15571

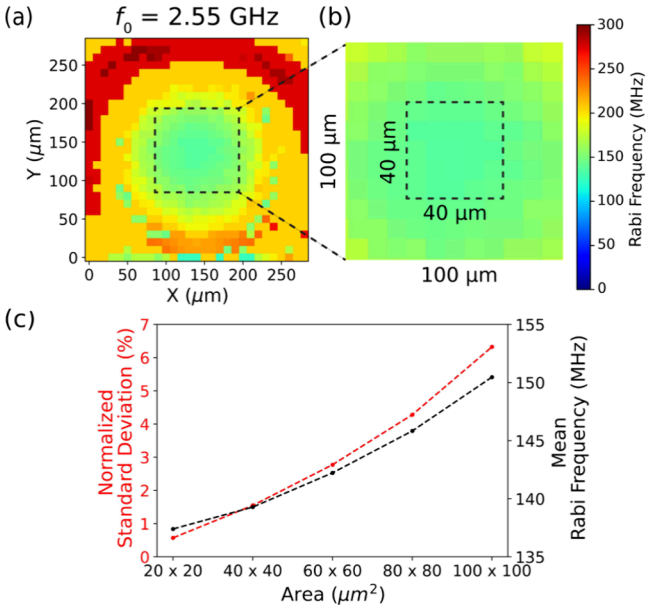



**Figure 3.** (a) NV-measured map of $f_1$ across a 280 $\mu$m × 280 $\mu$m area surrounding the innermost turn at $f_0$ = 2.55 GHz, with $\phi$ tuned for the maximal $f_1$ of 136.3 MHz at the loop center. (b) Zoomed 100 $\mu$m × 100 $\mu$m area (dashed box in panel (a)). (c) Mean and normalized standard deviation of $f_1$ vs window size centered on the loop center with $f_0$ = 2.55 GHz, obtained from the $f_1$ map in panel (a). The normalized standard deviation is about 1.5% within the 40 $\mu$m × 40 $\mu$m region.

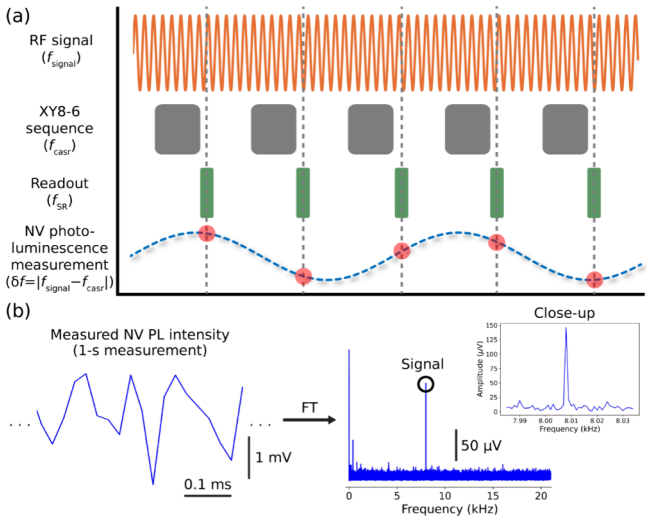



**Figure 4.** (a) CASR timing diagram for NV ensemble detection of a 29.992-MHz ($f_{signal}$) RF magnetic field from a test coil. NV electronic spins are driven at $f_0$ = 2.55 GHz ($B_0$ = 116 G)—with the maximal $f_1$ of 136.3 MHz—using alternating application of an XY8-6 dynamical decoupling sequence and NV PL readout. The CASR protocol produces an oscillatory variation in NV PL at frequency $\delta f = f_{signal} - f_{casr}$, where $f_{casr} \approx 30$ MHz is the central frequency used in the XY8-6 sequence. (b) Example measured NV PL intensity trace (left) and its Fourier transform (right), showing a peak at 8.008 kHz, in good agreement with expectations given the 1 ppm error of the signal generator used in this measurement.

synchronized readout (CASR),[10,11] a quantum spectroscopy protocol that alternates dynamical decoupling and optical readout of the NV electronic spins to provide Hz-scale spectral resolution (Figure 4a). We perform the measurements at $f_0$ = 2.55 GHz ($B_0$ = 116 G), with optimal phase ($\phi$) tuning yielding the maximum $f_1$ of 136.3 MHz, which is sufficiently large to enable phase-coherent measurements of the 29.992 MHz RF test signal.[8−12] The NV CASR measurement uses an XY8-6 sequence with a central frequency $f_{casr} \approx 30$ MHz. The CASR protocol effectively down-converts the RF signal frequency, and we observe an oscillatory variation in NV photoluminescence (PL) intensity at the down-converted frequency of $\delta f \approx 30$ MHz − 29.992 MHz = 8 kHz. The Fourier transform of observed PL time-domain signal (Figure 4b, left), measured for 1 s, shows a signal peak at 8.008 kHz (Figure 4b, right), with the 8 Hz deviation from 8 kHz being well less than the 1 ppm error of the RF signal generator (Rigol, Model DG 1032). Increasing the CASR measurement time from 1 s to 10 s to 100 s, the spectral resolution of the RF test signal improves from about 1 Hz to 0.1 Hz to 50 mHz, eventually limited by drift in the system (Figure S11).

This work demonstrates an approach to realize high Rabi frequency for a dense NV ensemble at the micrometer scale, with good spatial homogeneity, by increasing a microwave magnetic field in the center of a multiturn wire loop with careful microwave engineering, instead of relying on proximity to the loop. Specifically, at an NV driving frequency of 2.55 GHz ($B_0$ = 116 G), we achieve a 136.3 MHz NV Rabi frequency with 1.5% inhomogeneity over a 40 $\mu$m × 40 $\mu$m diamond area. We demonstrate the utility of our approach by using the NV ensemble in this diamond area to detect a ∼30-MHz magnetic signal with Hz-scale spectral resolution. This capability may benefit high Rabi frequency applications that employ a micrometer-scale ensemble of NV electronic spins, such as tesla-scale NV-NMR, although significant additional engineering challenges remain for NV-NMR at such high bias magnetic fields. In envisioned future work, a driver amplifier will be custom-designed with a microwave loop in the same chip and will be fabricated using a high-bandgap semiconductor (e.g., GaN) technology, such that the microwave current is further increased due to both the short distance between the active and passive circuits and also their codesign.

## ■ ASSOCIATED CONTENT

### Supporting Information

The Supporting Information is available free of charge at https://pubs.acs.org/doi/10.1021/acs.nanolett.5c03811.

Methods, comparison of device used in present work to several other works in the literature, optical setup for NV excitation and detection, experimental setup, simulation of the 3-turn primary loop with and without the open-circuited outer secondary loop, circuit model of the microwave signal pathway using the 50-Ω termination, 1-port *s*-parameter measurement and impedance analysis, NV ODMR and Rabi oscillation measurements at various $f_0$ values, ODMR spectrum under low microwave power at $f_0$ = 2.52 GHz, output power of the ZHL-25W-63+ power amplifier as a function of microwave excitation frequency, $f_1$ measurements at varying distances from the center of the 3-turn loop for the NV-measured maps of $f_1$ at $f_0$ = 2.55 GHz and $f_0$ = 6.02 GHz, determination of the spectral resolution for the CASR measurement shown in Figure 4 at varying measurement times (PDF)



https://doi.org/10.1021/acs.nanolett.5c03811
Nano Lett. 2025, 25, 15566−15571

## AUTHOR INFORMATION


### Corresponding Authors

**Donhee Ham** − *John A. Paulson School of Engineering and Applied Sciences, Harvard University, Cambridge, Massachusetts 02138, United States*; Email: donhee@seas.harvard.edu

**Ronald L. Walsworth** − *Quantum Technology Center, University of Maryland, College Park, Maryland 20742, United States; Department of Physics, Joint Quantum Institute, and Department of Electrical and Computer Engineering, University of Maryland, College Park, Maryland 20742, United States*; Email: walsworth@umd.edu

### Authors

**Han Sae Jung** − *John A. Paulson School of Engineering and Applied Sciences, Harvard University, Cambridge, Massachusetts 02138, United States*; orcid.org/0000-0003-3251-9790

**Johannes Cremer** − *Quantum Technology Center, University of Maryland, College Park, Maryland 20742, United States*

**Aoyang Zhang** − *John A. Paulson School of Engineering and Applied Sciences, Harvard University, Cambridge, Massachusetts 02138, United States; School of Integrated Circuits, Tsinghua University, Beijing 100084, China;* Present Address: For Aoyang Zhang : now with School of Integrated Circuits, Tsinghua University, Beijing 100084, China

**Shuhao Fan** − *John A. Paulson School of Engineering and Applied Sciences, Harvard University, Cambridge, Massachusetts 02138, United States*

**Sangha Kim** − *John A. Paulson School of Engineering and Applied Sciences, Harvard University, Cambridge, Massachusetts 02138, United States*

**Guang Yang** − *John A. Paulson School of Engineering and Applied Sciences, Harvard University, Cambridge, Massachusetts 02138, United States;* Present Address: For Guang Yang: now with the Anlyan Center, Yale University School of Medicine, New Haven, CT 06519, USA.

Complete contact information is available at: https://pubs.acs.org/10.1021/acs.nanolett.5c03811


### Author Contributions

○Authors H.S.J., J.C., and A.Z. contributed equally to this work. D.H. and R.L.W. conceived the work. H.S.J., J.C., S.K., and S.F. performed the experiments. A.Z. designed the 3-turn loop and the PCB. S.F. and A.Z. performed the s-parameter simulations. J.C., H.S.J., and A.Z. put together the measurement setup. H.S.J. and G.Y. packaged the chip. D.H. and R.L.W. supervised the project. H.S.J., J.C., A.Z., R.L.W., and D.H. wrote the manuscript, and all authors read and discussed it..

### Notes

The authors declare no competing financial interest.

## ACKNOWLEDGMENTS

This work was supported by the Gordon and Betty Moore Foundation, under Contract No. 7797.01; the Advanced Research Projects Agency-Energy (ARPA-E; Program Directors, Dr. Isik Kizilyalli and Dr. Olga Spahn), under Contract No. DE-AR0001063; the U.S. Army Research Laboratory, under Contract No. W911NF2420143; and the University of Maryland Quantum Technology Center.

## REFERENCES


(1) Balasubramanian, G.; Neumann, P.; Twitchen, D.; Markham, M.; Kolesov, R.; Mizuochi, N.; Isoya, J.; Achard, J.; Beck, J.; Tissler, J.; et al. Ultralong spin coherence time in isotopically engineered diamond. *Nat. Mater.* **2009**, *8*, 383−387.

(2) Bar-Gill, N.; Pham, L. M.; Jarmola, A.; Budker, D.; Walsworth, R. L. Solid-state electronic spin coherence time approaching one second. *Nat. Commun.* **2013**, *4*, 1743.

(3) Fuchs, G. D.; Dobrovitski, V. V.; Toyli, D. M.; Heremans, F. J.; Awschalom, D. D. Gigahertz dynamics of a strongly driven single quantum spin. *Science* **2009**, *326*, 1520−1522.

(4) Bayat, K.; Choy, J.; Baroughi, M. F.; Meesala, S.; Loncar, M. Efficient, uniform, and large area microwave magnetic coupling to NV centers in diamond using double split-ring resonators. *Nano Lett.* **2014**, *14* (3), 1208−1213.

(5) Sasaki, K.; Monnai, Y.; Saijo, S.; Fujita, R.; Watanabe, H.; Ishi-Hayase, J.; Itoh, K. M.; Abe, E. Broadband, large-area microwave antenna for optically detected magnetic resonance of nitrogen-vacancy centers in diamond. *Rev. Sci. Instrum.* **2016**, *87*, 053904.

(6) Mariani, G.; Nomoto, S.; Kashiwaya, S.; Nomura, S. System for the remote control and imaging of MW fields for spin manipulation in NV centers in diamond. *Sci. Rep.* **2020**, *10*, 4813.

(7) Yaroshenko, V.; Soshenko, V.; Vorobyov, V.; Bolshedvorskii, S.; Nenasheva, E.; Kotel'nikov, I.; Akimov, A.; Kapitanova, P. Circularly polarized microwave antenna for nitrogen vacancy centers in diamond. *Rev. Sci. Instrum.* **2020**, *91*, 035003.

(8) Mamin, H. J.; Kim, M.; Sherwood, M. H.; Rettner, C. T.; Ohno, K.; Awschalom, D. D.; Rugar, D. Nanoscale nuclear magnetic resonance with a nitrogen-vacancy spin sensor. *Science* **2013**, *339*, 557−560.

(9) Staudacher, T.; Shi, F.; Pezzagna, S.; Meijer, J.; Du, J.; Meriles, C. A.; Reinhard, F.; Wrachtrup, J. Nuclear magnetic resonance spectroscopy on a (5-nanometer)$^3$ sample volume. *Science* **2013**, *339*, 561−563.

(10) Glenn, D. R.; Bucher, D. B.; Lee, J.; Lukin, M. D.; Park, H.; Walsworth, R. L. High-resolution magnetic resonance spectroscopy using a solid-state spin sensor. *Nature* **2018**, *555*, 351−354.

(11) Bucher, D. B.; Glenn, D. R.; Park, H.; Lukin, M. D.; Walsworth, R. L. Hyperpolarization-enhanced NMR spectroscopy with femtomole sensitivity using quantum defects in diamond. *Phys. Rev. X* **2020**, *10*, 021053.

(12) Arunkumar, N.; Olsson, K. S.; Oon, J. T.; Hart, C. A.; Bucher, D. B.; Glenn, D. R.; Lukin, M. D.; Park, H.; Ham, D.; Walsworth, R. L. Quantum logic enhanced sensing in solid-state spin ensembles. *Phys. Rev. Lett.* **2023**, *131*, 100801.

(13) Mousoulis, C.; Xu, X.; Reiter, D. A.; Neu, C. P. Single cell spectroscopy: noninvasive measures of small-scale structure and function. *Methods* **2013**, *64*, 119−128.

(14) Grisi, M.; Vincent, F.; Volpe, B.; Guidetti, R.; Harris, N.; Beck, A.; Boero, G. NMR spectroscopy of single sub-nL ova with inductive ultra-compact single-chip probes. *Sci. Rep.* **2017**, *7*, 44670.

(15) Grant, S. C.; Aiken, N. R.; Plant, H. D.; Gibbs, S.; Mareci, T. H.; Webb, A. G.; Blackband, S. J. NMR spectroscopy of single neurons. *Magn. Reson. Med.* **2000**, *44*, 19−22.




https://doi.org/10.1021/acs.nanolett.5c03811
*Nano Lett.* 2025, 25, 15566−15571